The shape and dynamics of a heliotropic dusty ringlet in the Cassini Division

M.M. Hedman[a], J.A. Burt[a,b], J.A. Burns[a,c], M.S. Tiscareno[a]

[a] *Department of Astronomy, Cornell Unviersity, Ithaca NY 14853*

[b] *Department of Astronomy and Astrophysics, University of California, Santa Cruz, CA 95064*

[c] *College of Engineering, Cornell University, Ithaca NY 14853*

Keywords: Celestial Mechanics; Planetary Dynamics; Planetary Rings; Saturn, rings

Corresponding Author: Matthew Hedman
Space Sciences Building
Cornell University
Ithaca NY 14853
607-255-5913
mmhedman@astro.cornell.edu

The so-called "Charming Ringlet" (R/2006 S3) is a low-optical-depth, dusty ringlet located in the Laplace gap in the Cassini Division, roughly 119,940 km from Saturn center. This ringlet is particularly interesting because its radial position varies systematically with longitude relative to the Sun in such a way that the ringlet's geometric center appears to be displaced away from Saturn's center in a direction roughly toward the Sun. In other words, the ringlet is always found at greater distances from the planet's center at longitudes near the sub-solar longitude than it is at longitudes near Saturn's shadow. This "heliotropic" behavior indicates that the dynamics of the particles in this ring are being influenced by solar radiation pressure. In order to investigate this phenomenon, which has been predicted theoretically but not observed this clearly, we analyze multiple image sequences of this ringlet obtained by the Cassini spacecraft in order to constrain its shape and orientation. These data can be fit reasonably well with a model in which both the eccentricity and the inclination of the ringlet have "forced" components (that maintain a fixed orientation relative to the Sun) as well as "free" components (that drift around the planet at steady rates determined by Saturn's oblateness). The best-fit value for the eccentricity forced by the Sun is 0.000142 ± 0.000004, assuming this component of the eccentricity has its pericenter perfectly anti-aligned with the Sun. These data also place an upper limit on a forced inclination of $0.0007°$. Assuming the forced inclination is zero and the forced eccentricity vector is aligned with the anti-solar direction, the best-fit values for the free components of the eccentricity and inclination are 0.000066 ± 0.000003 and $0.0014 \pm 0.0001°$, respectively. While the magnitude of the forced eccentricity is roughly consistent with theoretical expectations for radiation pressure acting on 10-to-100-micron-wide icy grains, the existence of significant free eccentricities and inclinations poses a significant challenge for models of low-optical-depth dusty rings.

1. Introduction

Images taken by the cameras onboard the Cassini spacecraft have revealed that several of the wider gaps in Saturn's main rings contain low-optical-depth, dusty ringlets (Porco *et al.* 2005). One of these ringlets is located in the 200-km wide space in the outer Cassini Division between the inner edges of the Laplace Gap and the Laplace Ringlet, 119,940 km from Saturn's center. This ringlet has a peak normal optical depth of around 10^{-3} and its photometric properties (such as a dramatic increase in brightness at high phase angles) indicate that it is composed primarily of small dust grains less than 100 microns across (Horányi *et al.* 2009). While this feature is officially designated R/2006 S3 (Porco*et al.* 2006), it is unofficially called the "Charming Ringlet" by various Cassini scientists, and we will use that name here. Regardless of its name, this ringlet is of special interest because its radial position varies systematically with longitude relative to the Sun in such a way that the ringlet's geometric center appears to be displaced away from Saturn's center towards the Sun. In other words, this ringlet always appears some tens of kilometers further from the planet's center at longitudes near the sub-solar longitude than it is at longitudes near Saturn's shadow (see Figure 1). This "heliotropic" behavior suggests that non-gravitational

forces such as solar radiation pressure are affecting the particles' orbital dynamics, as predicted by various theoretical models (e.g. Horányi and Burns 1991, Hamilton 1993).

While other dusty ringlets, like those in the Encke Gap, may also show heliotropic behavior (Hedman *et al.* 2007), the Charming Ringlet provides the best opportunity to begin investigations of this phenomenon. Unlike the Encke Gap ringlets, the Charming Ringlet does not appear to contain bright clumps or noticeable short-wavelength "kinks" in its radial position. The absence of such features makes the global shape of the ringlet easier to observe and quantify. Furthermore, the radial positions of the edges of the Laplace gap and ringlet only vary by a few kilometers (Hedman *et al.* 2010), so this gap is a much simpler environment than other gaps (like the Huygens gap) where the radial locations of the edges can vary by tens of kilometers. Finally, the observations of the Charming Ringlet are more extensive than those of some other dusty ringlets.

In this paper, we build upon the preliminary work reported in Hedman *et al.* (2007) and Burt *et al.* (2008) in order to develop a model for the three-dimensional shape and orientation of the Charming Ringlet and to explore what such a model implies about the particle dynamics in this ring. First, we provide a brief summary of the data that will be used in this analysis and then fit the different data sets to models of an eccentric, inclined ringlet. These fits indicate that the shape and orientation of the ringlet change significantly over time. Next, we review the theoretical predictions for how particle orbits should behave under the influence of solar radiation pressure. Based on this theory, we develop a global model that includes both forced and free components in the ringlet's eccentricity and inclination; these can reproduce the observations reasonably well. Finally, we discuss the implications of such a model for the dynamics of this ringlet.

2. Observations and data reduction

All the images used in this analysis were obtained by the Narrow-Angle Camera (NAC) of the Imaging Science Subsystem (ISS) onboard the Cassini spacecraft (Porco *et al.* 2004). While ISS has obtained many images of the Charming Ringlet over the course of the Cassini mission, we will focus here exclusively on a limited sub-set of these data from a few imaging

Table 1: Data sets used in this analysis

(a) Longitudinal-scan observations used in this analysis

Orbit/Obs. Sequence	Date	Images	Radial resolution	Phase	Elevation	Sub-Spacecraft longitude	Subsolar latitude	Subsolar longitude	Observed longitude
030/AZDKMRHPH001/	2006-290	N1539746533-N1539760916 (59)	12-21 km/pixel	153-157°	35.5-40.1°	357.4-358.4°	-15.4°	191.3°	104.8-341.9°
042/RETMDRESA001/	2007-099	N1554850367-N1554852347 (10)	5-9 km/pixel	7-19°	(-21.3)-(-18.7)°	205.8-206.4°	-13.0°	197.3°	67.2-342.4°
070/RETMDRESA001/	2008-151	N1590852409-N1590863423 (46)	7-12 km/pixel	30-35°	21.4-26.9°	201.6-202.1°	-6.7°	211.0°	132.4-350.1°
071/PAZSCN002/	2008-159	N1591528309-N1591548903 (93)	5-9 km/pixel	41-44°	34.2-37.5°	204.7-206.3°	-6.6°	211.2°	91.5-233.4°
082/RETARMRLP001/	2008-237	N1598292162-N1598301617 (40)	6-10 km/pixel	36-45°	30.9-38.8°	204.2-205.0°	-5.4°	213.7°	67.0-359.0°
092/RETARMRLF001/	2008-312	N1604731407-N1604737767 (39)	5-8 km/pixel	46-56°	41.9-52.1°	214.3-215.4°	-4.3°	216.0°	72.1-357.1°
096/RETARMRMP001/	2008-343	N1607440846-N1607445736 (26)	4-6 km/pixel	57-74°	53.9-70.1°	224.9-228.1°	-3.8°	217.0°	77.4-364.7°

(b)Elevation-scan observations used in this analysis

Orbit/Obs. Sequence	Date	Images	Radial resolution	Phase	Elevation	Sub-Spacecraft longitude	Subsolar latitude	Subsolar longitude	Observed longitude
037/RPXMOVIE001/	2007-017	N1547739487-N1547782929 (34)	5-6 km/pixel	32-47°	(-8.7)-(+8.1)°	218.6-228.5°	-14.1°	194.5°	130-150°

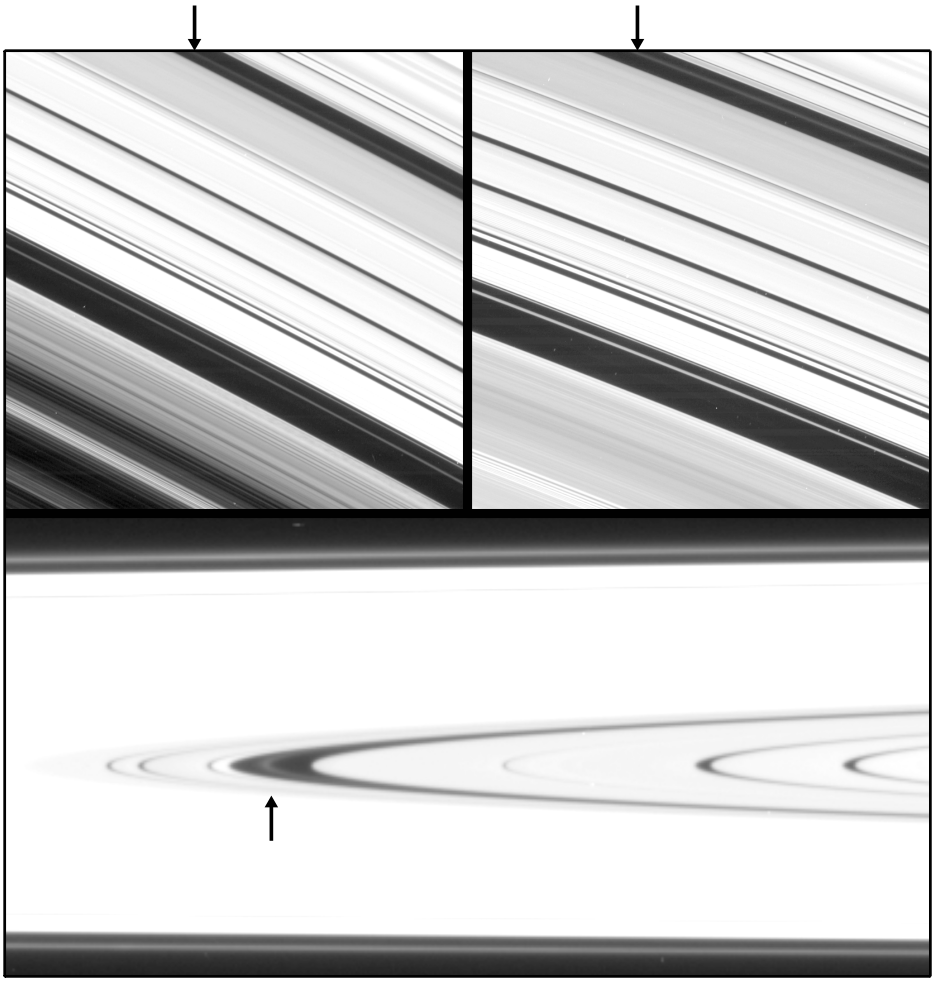

Fig. 1.— Sample images of the Charming Ringlet in the Cassini Division obtained by the narrow-angle camera onboard the Cassini spacecraft. The top two images were obtained on day 343 of 2008 as part of the RETARMRMP observation in Orbit 96, when the sub-solar longitude was 217° (see Table 1). The two images have been separately cropped, rotated and stretched to facilitate comparisons. In both images, radius in the rings increases towards to upper right. The arrows at the top of the image point to the Charming Ringlet in the Laplace gap. Note that in the left-hand image (N1607440846, observed longitude=5°) of a region near Saturn's shadow, the ringlet is closer to the inner edge of the gap, while in the right-hand image (N1609443806, observed longitude=192°) of a region near to the sub-solar longitude, the ringlet is closer to the outer edge of the gap. The bottom image (N1547759879) was obtained on day 17 of 2007 as part of the RPXMOVIE observation in Orbit 37, when the ring opening angle was only -0.36°. The image has been rotated so that Saturn's north pole points upwards. Ring radius increases from right to left, and the arrow points to the Charming Ringlet in the Laplace Gap. Note that the ringlet appears slightly displaced upwards in this image relative to the edges of the gap (the upper arm of the ring disappears into the glare of the edge of the gap faster than the lower arm). This suggests that this ringlet is inclined.

sequences. Each of these sequences was obtained over a relatively short period of time and covers a sufficient range of longitudes or viewing geometries that it can provide useful constraints on the shape and orientation of the ring. These data sets are therefore particularly useful for developing a shape model for this ring. In principle, once a rough model has been established, additional data can be used to refine the model parameters and test the model. However, such an analysis is beyond the scope of this paper and therefore will be the subject of future work.

Two different types of observation sequences will be utilized in the present study, "longitudinal scans" and "elevation scans". Each longitudinal scan consists of a series of images of the Cassini Division, with different images centered at different inertial longitudes in the rings. These scans provide maps of the apparent radial position of the Charming Ringlet as a function of longitude relative to the Sun. The seven such scans used in this analysis (listed in Table 1a) are all the scans obtained prior to 2009 that contain the Charming Ringlet, have sufficient radial resolution to clearly resolve the ringlet and also cover a sufficiently broad range of longitudes ($> 140°$) to provide a reliable measurement of both the ringlet's eccentricity and inclination (see below).

By contrast, elevation scans consist of a series of images of the ring ansa taken over a period of time when the spacecraft passed through the ring-plane, yielding observations covering a range of ring-opening angles B around zero. Such images provide limited information about the ringlet's eccentricity, however, observable shifts in the ringlet's apparent position relative to other ring features provide evidence that the ringlet is inclined (see Fig 1). These observations therefore can furnish additional constraints on the ringlet's vertical structure. Thus far, only one image sequence (given in Table 1b) has sufficient resolution and elevation-angle coverage to yield useful constraints on the ringlet's orientation.

All of these images were processed using the standard CISSCAL calibration routines (version 3.6) (Porco *et al.* 2004) that remove backgrounds, flat-field the images, and convert the raw data numbers into I/F (a standardized measure of reflectance where I is the intensity of the scattered radiation while πF is the solar flux at Saturn). We then extracted measurements of the ringlet's radial position with the following procedures.

First, all the relevant images were geometrically navigated employing the appropriate SPICE kernels to establish the position and approximate pointing of the spacecraft. The pointing was refined using the outer edge of the Jeffreys Gap (called OEG 15 in French *et al.* 1993, assumed to be circular and lie at 118,968 km) as a fiducial feature. Recent Cassini occultation measurements demonstrate that this feature is circular to better than 1 km (Hedman *et al.* 2010; French *et al.* 2010), making it a reliable reference point in the rings.

Once each image was navigated, the brightness data were converted into radial brightness profiles by averaging the brightness at each radius over a range of longitudes. For the longitudinal scans, each image covered a sufficiently small range of longitudes that variations in the radial position of the ringlet within an image could be ignored. Consequently, a single radial scan was derived from each image by averaging the data over all observed

longitudes. By contrast, for the elevation scans, variations in the radial position of the ringlet were apparent within individual images. A series of 8-20 radial brightness profiles was therefore extracted from each image, with each profile being the average brightness of the ring in a range of longitudes between 0.5° and 1.0° wide. Note that for all these profiles, the radius scale corresponds to the projected position of any given feature onto the ring-plane.

The Charming Ringlet could be detected as a brightness peak within the Laplace gap in all of these radial scans. The radial position of the ringlet was estimated from each scan by fitting the ringlet's brightness profile to a Gaussian. For the high-phase observations in Orbit 30, the ringlet was sufficiently bright that the Gaussian could be fit directly to the radial profile. For the other (lower-phase) profiles, however, the ringlet was considerably fainter and the brightness variations within the gap due to various instrumental effects could not be ignored. In these situations, a background light profile for the gap was computed using the data outside the ringlet (the edges of the ringlet were determined based on where the slope of the brightness profile around the ringlet was closest to zero). This background was interpolated into the region under the ringlet (using a spline interpolation of the profile smoothed over three radial bins) and a Gaussian was fit to the background-subtracted ringlet profile. Figure 2 shows examples of the raw profile, the interpolated background and the background plus the fitted Gaussian, demonstrating that this procedure yields sensible results even when the ringlet is rather subtle.

The above process yielded a series of measurements of the apparent radial position of the ringlet as a function of longitude. Figure 3 shows these data for the seven different longitudinal scans. Note that in all cases the ringlet is found furthest from the planet at a point near to the sub-solar longitude. This is not just a coincidence of when the ringlet was observed, but is instead the evidence for the "heliotropic" character of this ringlet. However, we can also observe that the apparent shape of the ringlet varies significantly among the different observations. This implies that the ringlet does not simply maintain a fixed orientation relative to the Sun, but instead has a more complex and time-variable shape.

For the elevation scan, the radial position of the ringlet versus longitude from each image can be fit to a line. Figure 4 shows the slopes of the line derived from these images as a function of ring-opening angle B. The slope changes dramatically as the spacecraft crosses the ringplane. This strongly suggests that this portion of the ring is vertically displaced from the ringplane (Burt *et al.* 2008), and means that we will need a three-dimensional model to fully describe the shape of this ringlet.

3. Ringlet shape estimates from individual observations

The above evidence for time-variable and three-dimensional structure obviously complicates our efforts to quantify the Charming Ringlet's shape. Fortunately, it turns out that the data from individual scans can be reasonably well fit by simple models of eccentric,

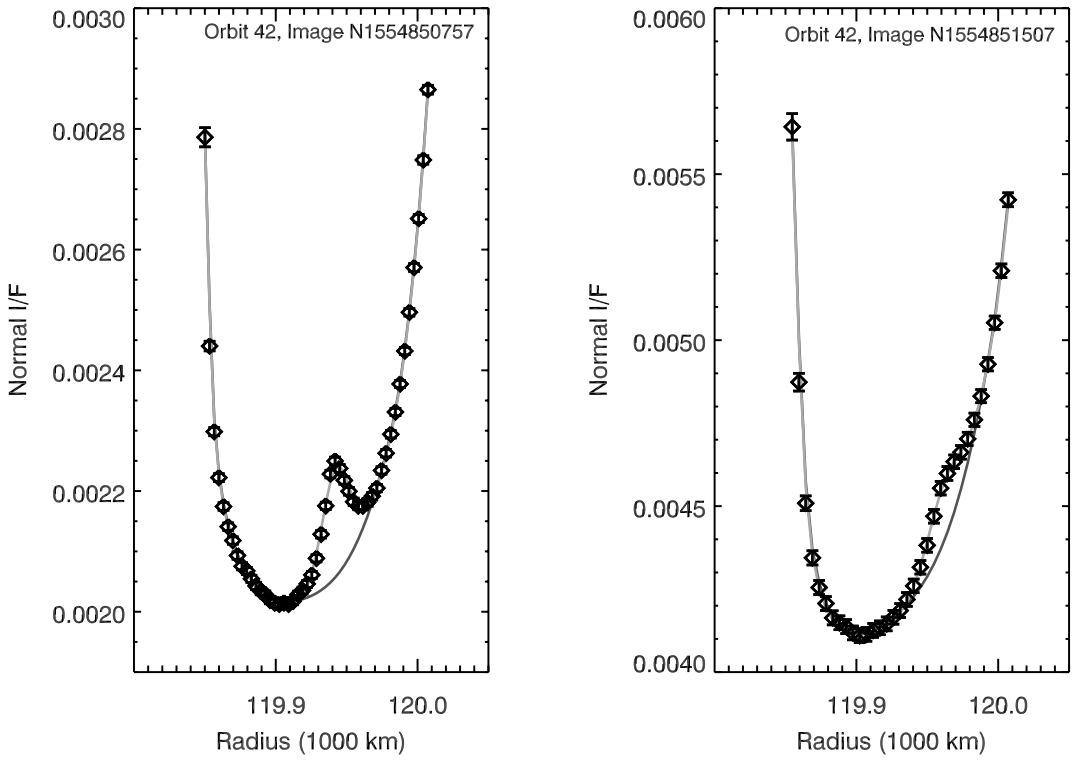

Fig. 2.— Examples of the profile fitting procedures described in the text. In each plot, the data points shows the brightness profile across the Laplace Gap, including the Charming Ringlet. The data are given in terms of 'Normal I/F', which is the observed I/F multiplied by the sine of the ring opening angle. The dark grey curve shows the fit background profile, while the light grey curve shows this background plus the best-fit gaussian profile for the ringlet. Note the example on the right is among the most extreme in terms of the subtleness of the ring signal, and even here the fit is very good. Most of the fits used in this analysis are more like the example on the left.

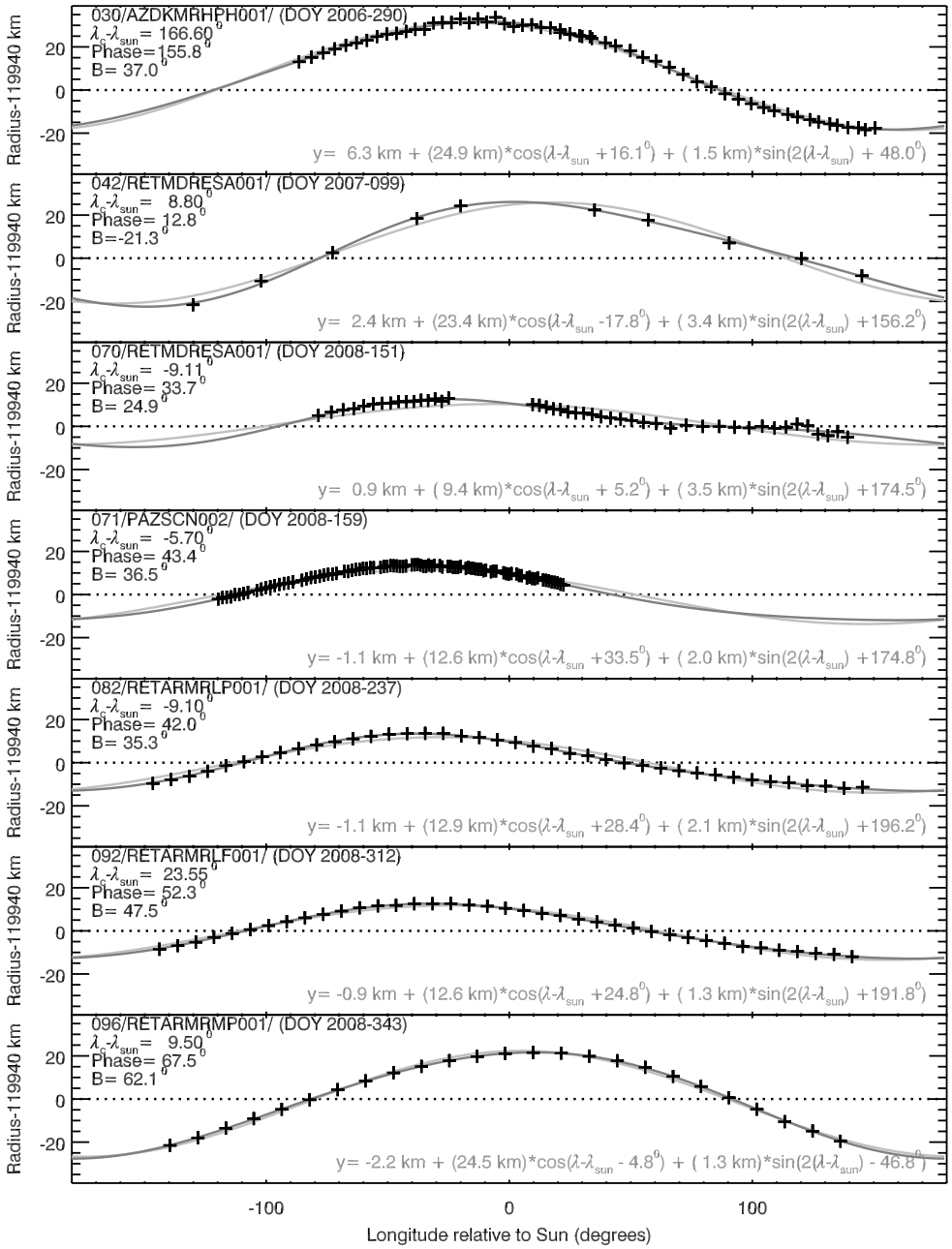

Fig. 3.— The apparent radius of the Charming Ringlet (projected onto the ring-plane) as a function of longitude relative to the Sun, derived from the seven longitudinal scans. The observations are shown as crosses. The dark grey curve shows the best-fit model to each data set with the parameters listed on each plot (compare with Eq. 5). The light grey curve is the same model with the term $\propto \sin(2\lambda)$ removed to illustrate the importance of this term to the overall fit.

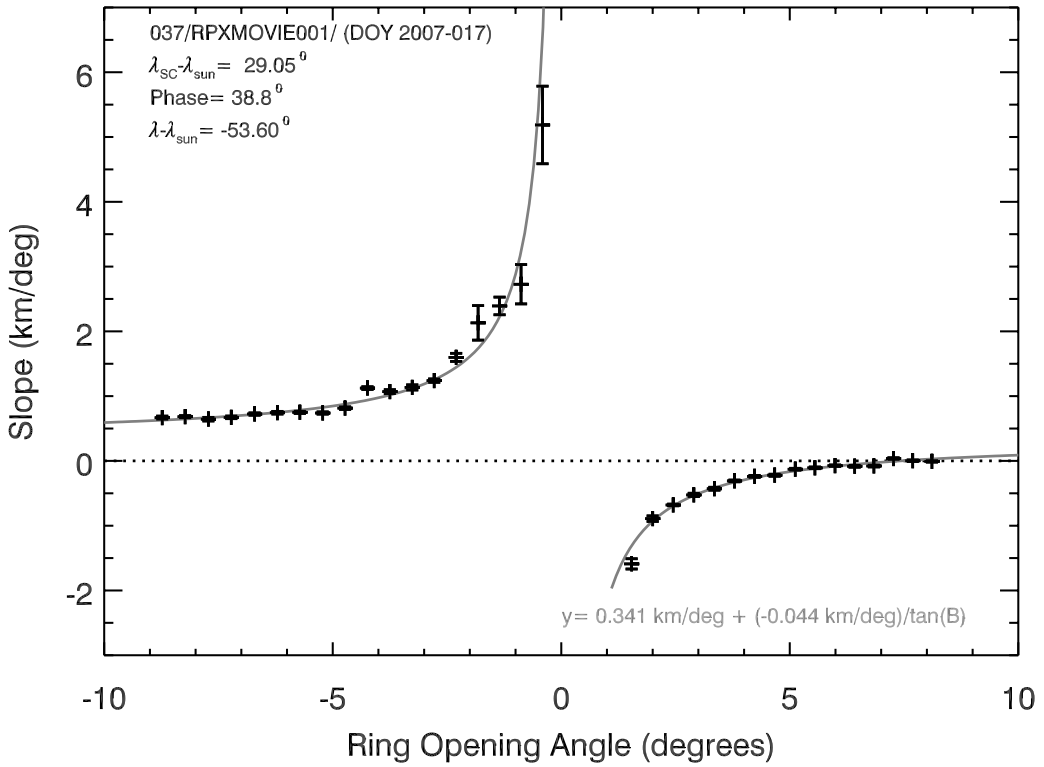

Fig. 4.— The slope in the apparent radius versus longitude, plotted against ring-opening angle B to the spacecraft, as derived from the single elevation scan. The curve is the best-fitting model with the parameters shown (compare with Eq. 6).

inclined ringlets. By fitting each scan to such a model, we can further reduce the data to a small number of shape/orbital parameters, which may change with time.

Each scan consists of measurements of the apparent radial position of the ringlet projected on the ringplane $\tilde{r}$ versus longitude relative to the Sun $\lambda - \lambda_\odot = \lambda'$. Assuming the ringlet can have both an inclination and an eccentricity, the radial and vertical positions of the ringlet versus longitude are for small eccentricities and inclinations well approximated by:

$$r = a - ae\cos(\lambda' - \varpi') \tag{1}$$

$$z = ai\sin(\lambda' - \Omega'), \tag{2}$$

where a, e and i are the semi-major axis, eccentricity and inclination of the ringlet, and ϖ' and Ω' are the longitudes of pericenter and ascending node relative to the Sun.

If z is nonzero, the apparent position of the ringlet will be displaced when it is projected onto the ringplane. Assuming the observer is sufficiently far from the ring, this displacement is simply

$$\delta\tilde{r} = -\frac{z}{\tan B}\cos(\lambda' - \lambda'_c), \tag{3}$$

where B is the ring opening angle to the observing spacecraft and λ'_c is the longitude of the spacecraft relative to the Sun. Substituting in the above value for z, we find:

$$\delta\tilde{r} = \frac{-ai}{2\tan B}[\sin(2\lambda' - \Omega' - \lambda'_c) - \sin(\Omega' - \lambda'_c)]. \tag{4}$$

The apparent radial position of such a ringlet is therefore:

$$\tilde{r} = r + \delta\tilde{r} = a + \frac{ai}{2\tan B}\sin(\Omega' - \lambda'_c) - ae\cos(\lambda' - \varpi') - \frac{ai}{2\tan B}\sin(2\lambda' - \Omega' - \lambda'_c). \tag{5}$$

Note that this expression contains two terms that depend on the longitude λ': one proportional to e and one proportional to i. Since these two terms depend on longitude in different ways, it should be possible to determine both the eccentricity and inclination from any observation sequence that covers a sufficiently broad range of longitudes. Also, since the terms involving i depend on the ring opening angle B while those involving e do not, the effects of inclination and eccentricity on the apparent position of the ringlet should also be separable when the observation sequences cover a sufficient range in B.

3.1. Elevation Scan

Over the limited range of longitudes observed in each image of the elevation scan, the apparent-radius-versus-longitude curve is well fit by a straight line. Figure 4 shows the slope of this line as a function of ring opening angle, with error bars derived from the linear fit.

Given the above expression (Eq. 5) for the apparent radial position of the ring versus longitude, these measured slopes can be identified with the quantity:

$$m = \frac{d\tilde{r}}{d\lambda'} = ae\sin(\lambda' - \varpi') - \frac{ai}{\tan B}\cos(2\lambda' - \Omega' - \lambda'_c) \tag{6}$$

In other words, $m = C - z/\tan B$, where C is the constant background slope due to the eccentricity of the ringlet and z is its vertical displacement at the observed longitude. Fitting the data from the elevation scan to an equation of this form, we find that at the observed longitude and time:

$$z = ai\cos(2\lambda' - \Omega' - \lambda'_c) = 2.54 \pm 0.02\,\mathrm{km}, \tag{7}$$

$$C = ae\sin(\lambda' - \varpi') = 19.5 \pm 0.2\,\mathrm{km}. \tag{8}$$

The curve plotted on Fig. 4 shows this best-fit function, which reproduces the trends in the data rather well. However, the χ^2 of this fit is 206 for 32 degrees of freedom, indicating that the errors on the individual slope measurements have been underestimated. Thus the above uncertainties on z and C should probably be increased by a factor of 2.5. Note that while these data alone cannot provide exact estimates on eccentricity and inclination, we can establish that ai is at least 2.5 km and ae is at least 19 km.

3.2. Longitudinal Scans

Figure 3 shows the estimated position of the Charming Ringlet versus longitude relative to the Sun for each of the seven longitudinal scans. Each of these data sets has been fit to a function of the form (cf Eq. 5)

$$\tilde{r} = r_o + r_1\cos(\lambda' - \phi_1) + r_2\cos(2\lambda' - \phi_2). \tag{9}$$

The best fit solutions, shown as the dark grey curves in Fig. 3, satisfactorily reproduce the trends seen in the real data. We can therefore use the parameters of this fit and Equation 5 to derive the ring-shape parameters a, e, i, ϖ' and Ω' (see Table 2). The error bars on the orbital parameters are computed using the rms residuals from the fit to estimate the error bars on each data point. These residuals are always less than one kilometer, or about a factor of 10 better than the image resolution (see Tables 1 and 2), and probably reflect small errors and uncertainties in the fitted locations of the fiducial edge and ringlet center. The small scatter in these data therefore confirms the stability of the pointing and fitting algorithms within each of these sequences.

Let us consider each of these different parameters in turn, starting with the semi-major axis a. No formal error bars on this parameter are given here because this parameter is the one most likely to be affected by systematic pointing uncertainties between the different scans caused by differences in the appearance and contrast of the fiducial edge. Nevertheless, the scatter in these values is still only a few kilometers and well below the resolutions of the images (compare to Table 1), providing further confirmation that the fitting procedures employed here are robust. Note that all the observations give a values within a few kilometers of 119,940 km, which is very close to exactly halfway between the inner edge of the Laplace Gap at 119,845 km and the inner edge of the Laplace ringlet at 120,036 km (Hedman *et al.* 2010).

Turning to the eccentricity and pericenter, we may note that while the pericenter is always around 180° from the Sun, both the pericenter location and the eccentricity vary significantly from one observation to another. The values of ae range from 9.5 km to 25 km, and the pericenter locations deviate from the anti-Sun direction by up to 35°. The ringlet therefore does not maintain a perfectly fixed orientation relative to the Sun.

Finally, consider the inclination and the node estimates. Six of the seven estimates for ai fall in a relatively narrow range of 2.3-3.2 km. The one outlier is the 5.1 km estimate from the Orbit 96 data. However, this observation was made while the spacecraft was well above the ringplane, and the ring opening angle changed more over the course of this observation than in any of the others (see Table 1). Thus this measurement of the inclination may be regarded as suspect. Looking at the remaining data, the relatively small scatter in ai may imply that the inclination of this ringlet does not vary much with time. However, we also find that the node positions are very widely scattered. This implies that this ringlet's line of nodes does not have a fixed orientation relative to the Sun.

4. Solar radiation pressure and models of heliotropic orbits

The above data show that the ringlet's pericenter is on average anti-aligned with the Sun, suggesting that a force like solar radiation pressure is influencing the shape and orientation of this ringlet. However, the eccentricity and alignment of this ringlet also vary significantly over time, and this indicates that the ringlet's dynamics are more complex than we might have expected. In order to facilitate the interpretation of these data, we will review how solar radiation pressure affects orbital parameters. This analysis roughly follows the treatment given in Horányi and Burns (1991) for a particle in orbit around Jupiter, but is generalized to account for the possibility that the Sun may be located significantly above or below the ringplane. Also, we will restrict ourselves to nearly circular orbits, thereby obtaining simpler expressions than those given by Hamilton (1993). Note that throughout this analysis we assume the dynamics of the particles is determined entirely by solar radiation pressure and Saturn's gravity (other non-gravitational forces such as plasma drag are

Table 2: Ring shape parameters derived from the longitudinal scans

Orbit/Obs. Sequence	rms^a (km)	δa^b (km)	ae (km)	$\varpi - \lambda_\odot$ (deg)	ai (km)	$\Omega - \lambda_\odot$ (deg)
030/AZDKMRHP001/	0.7	5.8	24.92±0.26	163.9±0.7	2.27±0.34	325.4±6.4
042/RETMDRESA001/	0.9	2.8	23.42±0.52	197.8±0.9	2.63±0.29	195.0±9.7
070/RETMDRESA001/	0.9	-0.4	9.42±0.61	174.8±2.9	3.21±0.35	14.6±5.3
071/PAZSCN002/	0.2	-1.7	12.59±0.95	146.5±1.3	3.01±0.51	10.9±3.6
082/RETARMRLP001/	0.3	-1.1	12.88±0.08	151.6±0.3	3.03±0.09	352.9±2.0
092/RETARMRLF001/	0.2	-0.6	12.59±0.06	155.2±0.2	2.75±0.09	349.3±2.5
096/RETARMRMP001/	0.2	-1.6	24.55±0.08	184.8±0.1	5.08±0.24	217.3±2.8

[a] rms residuals of the data after the fit.

[b] $a - 119940$ km

neglected).

We begin with the standard perturbation equations for the semi-major axis a, eccentricity e, inclination i, the longitude of periapse ϖ and the longitude of node Ω of a particle orbit (see e.g. Burns 1976). Since we are interested in orbits with small eccentricities and inclinations, these expressions can be approximated as

$$\frac{da}{dt} = 2an\left[\frac{F_r}{F_G}e\sin f + \frac{F_t}{F_G}(1+e\cos f)\right], \tag{10}$$

$$\frac{de}{dt} = n\left[\frac{F_r}{F_G}\sin f + 2\frac{F_t}{F_G}\cos f\right], \tag{11}$$

$$\frac{d\varpi}{dt} = \frac{n}{e}\left[-\frac{F_r}{F_G}\cos f + 2\frac{F_t}{F_G}\sin f\right], \tag{12}$$

$$\frac{di}{dt} = n\left[\frac{F_z}{F_G}\cos(\varpi-\Omega+f)\right], \tag{13}$$

$$\frac{d\Omega}{dt} = \frac{n}{\sin i}\left[\frac{F_z}{F_G}\sin(\varpi-\Omega+f)\right], \tag{14}$$

where n is the particle's mean motion, $F_G = GMm_g/a^2$ is approximately the force of Saturn's gravity on a particle with mass m_g (neglecting the effects of Saturn's finite oblateness), f is the particle's true anomaly and F_r, F_t and F_z are the radial, azimuthal and normal (to the orbit plane in the direction of orbital angular momentum) components of the perturbing force, respectively.

Say the Sun is located at an elevation angle $B_\odot$ above the rings and a longitude $\lambda_\odot$ in some inertial coordinate system. Then the components of the solar radiation pressure force $F_\odot$ at a specified longitude λ in the ring are given by:

$$F_z = -F_\odot \sin B_\odot, \tag{15}$$

$$F_r = -F_\odot \cos B_\odot \cos(\lambda-\lambda_\odot), \tag{16}$$

$$F_t = +F_\odot \cos B_\odot \sin(\lambda-\lambda_\odot). \tag{17}$$

Substituting these expressions into the equations of motion, and recognizing that $f = \lambda - \varpi$, we obtain

$$\frac{da}{dt} = 2an\frac{F_\odot \cos B_\odot}{F_G}[e\sin(\varpi-\lambda_\odot) + \sin(\lambda-\lambda_\odot)], \tag{18}$$

$$\frac{de}{dt} = n\frac{F_\odot \cos B_\odot}{2F_G}[3\sin(\varpi-\lambda_\odot) + \sin(2\lambda-\varpi-\lambda_\odot)], \tag{19}$$

$$\frac{d\varpi}{dt} = \frac{n}{e}\frac{F_\odot \cos B_\odot}{2F_G}[3\cos(\varpi-\lambda_\odot) - \cos(2\lambda-\varpi-\lambda_\odot)], \tag{20}$$

$$\frac{di}{dt} = -n\frac{F_\odot \sin B_\odot}{F_G}\cos(\lambda-\Omega), \tag{21}$$

$$\frac{d\Omega}{dt} = -\frac{n}{\sin i}\frac{F_\odot \sin B_\odot}{F_G}\sin(\lambda-\Omega). \tag{22}$$

For small perturbations, we expect that ϖ, Ω, e, i and $\lambda_\odot$ will change much more slowly than λ does. Thus, to obtain the long-term secular evolution of the orbital elements, we may average these expression over a single orbit. However, in doing this, we must take care to account for Saturn's shadow, which blocks the light from the Sun during a fraction of the particle's orbit ϵ. The appropriate orbit-averaged equations of motion are:

$$\left\langle \frac{da}{dt} \right\rangle = nae \left[2d(\epsilon) \frac{F_\odot \cos B_\odot}{F_G} \right] \sin(\varpi - \lambda_\odot), \tag{23}$$

$$\left\langle \frac{de}{dt} \right\rangle = n \left[\frac{3}{2} f(\epsilon) \frac{F_\odot \cos B_\odot}{F_G} \right] \sin(\varpi - \lambda_\odot), \tag{24}$$

$$\left\langle \frac{d\varpi}{dt} \right\rangle = \frac{n}{e} \left[\frac{3}{2} f(\epsilon) \frac{F_\odot \cos B_\odot}{F_G} \right] \cos(\varpi - \lambda_\odot), \tag{25}$$

$$\left\langle \frac{di}{dt} \right\rangle = -n \left[g(\epsilon) \frac{F_\odot \sin B_\odot}{F_G} \right] \cos(\Omega - \lambda_\odot), \tag{26}$$

$$\left\langle \frac{d\Omega}{dt} \right\rangle = \frac{n}{\sin i} \left[g(\epsilon) \frac{F_\odot \sin B_\odot}{F_G} \right] \sin(\Omega - \lambda_\odot). \tag{27}$$

where $d(\epsilon) = 1 - \epsilon$, $f(\epsilon) = 1 - \epsilon + \sin(2\pi\epsilon)/6\pi$ and $g(\epsilon) = \sin(\pi\epsilon)/\pi$ (see Appendix).

For an oblate planet like Saturn, these equations of motion are incomplete because they do not take into account the steady precession in the pericenter and node caused by the planet's finite oblateness, which augments the motion of ϖ and Ω. The full equations of motion are therefore:

$$\left\langle \frac{da}{dt} \right\rangle = nae \left[2d(\epsilon) \frac{F_\odot \cos B_\odot}{F_G} \right] \sin(\varpi - \lambda_\odot), \tag{28}$$

$$\left\langle \frac{de}{dt} \right\rangle = n \left[\frac{3}{2} f(\epsilon) \frac{F_\odot \cos B_\odot}{F_G} \right] \sin(\varpi - \lambda_\odot), \tag{29}$$

$$\left\langle \frac{d\varpi}{dt} \right\rangle = \frac{n}{e} \left[\frac{3}{2} f(\epsilon) \frac{F_\odot \cos B_\odot}{F_G} \right] \cos(\varpi - \lambda_\odot) + \dot{\varpi}_o, \tag{30}$$

$$\left\langle \frac{di}{dt} \right\rangle = -n \left[g(\epsilon) \frac{F_\odot \sin B_\odot}{F_G} \right] \cos(\Omega - \lambda_\odot), \tag{31}$$

$$\left\langle \frac{d\Omega}{dt} \right\rangle = \frac{n}{\sin i} \left[g(\epsilon) \frac{F_\odot \sin B_\odot}{F_G} \right] \sin(\Omega - \lambda_\odot) + \dot{\Omega}_o, \tag{32}$$

where $\dot{\varpi}_o$ and $\dot{\Omega}_o$ are pericenter precession and nodal regression rates due to Saturn's oblateness.

Finally, we can simplify these expressions by replacing the inertial longitudes ϖ and Ω with longitudes measured relative to the Sun, $\varpi' = \varpi - \lambda_\odot$ and $\Omega' = \Omega - \lambda_\odot$:

$$\left\langle \frac{da}{dt} \right\rangle = nae \left[2d(\epsilon) \frac{F_\odot \cos B_\odot}{F_G} \right] \sin \varpi', \tag{33}$$

$$\left\langle \frac{de}{dt} \right\rangle = n \left[\frac{3}{2} f(\epsilon) \frac{F_\odot \cos B_\odot}{F_G} \right] \sin \varpi', \tag{34}$$

$$\left\langle \frac{d\varpi'}{dt} \right\rangle = \frac{n}{e}\left[\frac{3}{2}f(\epsilon)\frac{F_\odot \cos B_\odot}{F_G}\right]\cos\varpi' + \dot{\varpi}'_o, \tag{35}$$

$$\left\langle \frac{di}{dt} \right\rangle = -n\left[g(\epsilon)\frac{F_\odot \sin B_\odot}{F_G}\right]\cos\Omega', \tag{36}$$

$$\left\langle \frac{d\Omega'}{dt} \right\rangle = \frac{n}{\sin i}\left[g(\epsilon)\frac{F_\odot \sin B_\odot}{F_G}\right]\sin\Omega' + \dot{\Omega}'_o, \tag{37}$$

where $\dot{\varpi}'_o = \dot{\varpi}_o - \dot{\lambda}_\odot$ and $\dot{\Omega}'_o = \dot{\Omega}_o - \dot{\lambda}_\odot$ will be referred to here as the "modified" pericenter precession and nodal regression rates, respectively.

Assuming that $B_\odot$ changes sufficiently slowly, then for any semi-major axis a there is a unique steady-state solution to these equations where $\left\langle \frac{da}{dt} \right\rangle = \left\langle \frac{de}{dt} \right\rangle = \left\langle \frac{d\varpi'}{dt} \right\rangle = \left\langle \frac{di}{dt} \right\rangle = \left\langle \frac{d\Omega'}{dt} \right\rangle = 0$. This steady-state orbital solution has the following orbital parameters (assuming $\sin i \simeq i$):

$$e_f = \frac{n}{\dot{\varpi}'_o}\left[\frac{3}{2}f(\epsilon)\frac{F_\odot}{F_G}\cos B_\odot\right], \tag{38}$$

$$\varpi_f = \lambda_\odot + \pi, \tag{39}$$

$$i_f = \frac{n}{|\dot{\Omega}'_o|}\left[g(\epsilon)\frac{F_\odot}{F_G}\sin|B_\odot|\right], \tag{40}$$

$$\Omega_f = \lambda_\odot + \frac{\pi}{2}\frac{B_\odot}{|B_\odot|}. \tag{41}$$

This orbit has a finite eccentricity e_f with the pericenter anti-aligned with the Sun, so that the apoapse of the orbit points towards the Sun. This is grossly consistent with the observed heliotropic behavior of the Charming Ringlet shown in Figs. 3 and 4. Furthermore, if $B_\odot$ is non-zero, then this orbit also has a finite inclination, and the ascending node is located $\pm 90^\circ$ from the sub-solar longitude, depending on whether the Sun is north or south of the ringplane. The orbit will therefore be inclined so that it is on the opposite side of the equator plane as the Sun at longitudes near local noon.

However, this steady-state solution is a special case. More general solutions to the equation of motion can be most clearly described using the variables (Horányi and Burns 1991, see also Murray and Dermott 1999, equations 7.18-7.19):

$$h = e\cos(\varpi - \lambda_\odot) = e\cos\varpi', \tag{42}$$

$$k = e\sin(\varpi - \lambda_\odot) = e\sin\varpi', \tag{43}$$

$$p = i\cos(\Omega - \lambda_\odot) = i\cos\Omega', \tag{44}$$

$$q = i\sin(\Omega - \lambda_\odot) = i\sin\Omega'. \tag{45}$$

In terms of these variables, the above equations of motion reduce to:

$$\left\langle \frac{da}{dt} \right\rangle = \frac{4d(\epsilon)}{3f(\epsilon)}ae_f\dot{\varpi}'_o k, \tag{46}$$

$$\left\langle \frac{dh}{dt} \right\rangle = -\dot{\varpi}'_o k, \tag{47}$$

$$\left\langle \frac{dk}{dt} \right\rangle = \dot{\varpi}'_o(h + e_f), \tag{48}$$

$$\left\langle \frac{dp}{dt} \right\rangle = -\dot{\Omega}'_o \left(q - i_f \frac{B_\odot}{|B_\odot|} \right), \tag{49}$$

$$\left\langle \frac{dq}{dt} \right\rangle = \dot{\Omega}'_o p, \tag{50}$$

where e_f and i_f are the steady-state (forced) eccentricity and inclination derived above. While both these parameters depend on the semi-major axis a via the mean-motion n, Eqn 46 demonstrates that the fractional variations in the semi major axis are $\mathcal{O}(e^2)$ and can therefore be neglected for the nearly circular orbits of interest here. Thus for the rest of this analysis e_f and i_f will be assumed to be constants. In that case, $[h, k]$ and $[p, q]$ satisfy two pairs of separately coupled harmonic-oscillator equations, so the trajectories traced out by the above equations form circles in $[h, k]$ and $[p, q]$ space (Horányi and Burns 1991). The centers of these circles are given by the steady-state solutions, and the orbit evolves around the circles at rates given by the modified precession rates $\dot{\varpi}'_o$ and $\dot{\Omega}'_o$. As the orbit evolves along these paths, if e_f and i_f are nonzero, the orbit's total eccentricity and inclination will change periodically with periods of $2\pi/\dot{\varpi}'_o$ and $2\pi/\dot{\Omega}'_o$, respectively. In general, the various orbital parameters can be described as the vector sums in $[h, k]$ and $[p, q]$ space of two components: a constant, "forced" component and a time-variable, or "free" component. The evolution of such an orbit is specified by 10 parameters (see Fig 5):

- e_f and i_f, the so-called forced eccentricity and forced inclination, whose values should be determined by Saturn's gravity and the in-plane and normal components of the solar radiation pressure.
- $\varpi'_f = \varpi_f - \lambda_\odot$ and $\Omega'_f = \Omega_f - \lambda_\odot$, which specify the orientation of the orbit relative to the Sun. Given the above analysis, we expect $\varpi'_f = \pi$ and $\Omega'_f = \pm\pi/2$
- e_l and i_l, the so-called free eccentricity and free inclination. These are the radii of the circles traced out by the orbits in $[h, k]$ and $[p, q]$ space, respectively. These parameters can in principle have any non-negative value, and are set by the initial conditions.
- ϖ'_l and Ω'_l, the pericenter and node (relative to the Sun) of the free components of the eccentricity and inclination at some epoch time. These parameters are initial conditions and can in principle have any value between 0 and 2π.
- $\dot{\varpi}'_l$ and $\dot{\Omega}'_l$, which specify how fast the free components of the eccentricity and inclination move around the fixed points. These parameters should equal the modified precession and regression rates $\dot{\varpi}'_o$ and $\dot{\Omega}'_o$, which are determined by the oblateness of the planet and the motion of the Sun.

At this point, it is useful to examine heuristically the evolution of such orbits, to clarify the physical processes involved. In the case where the eccentricity equals e_f and has its pericenter anti-aligned with the sun, the orbit can be regarded as a circular path that is

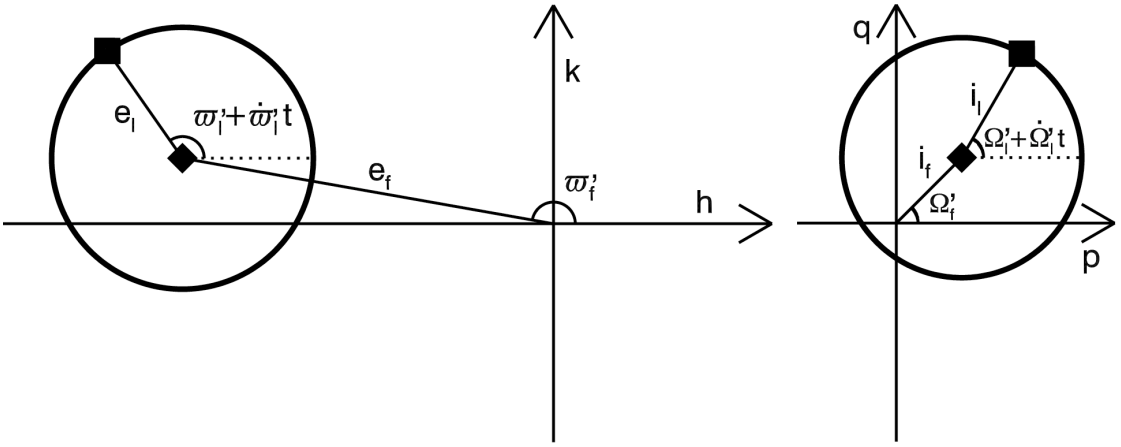

Fig. 5.— A graphical representation of the free and forced components of the eccentricity (left) and inclination (right), showing the parameters used in this analysis

displaced by a distance ae_f from Saturn's center. In this particular configuration, the orbit-averaged torque on the particle from solar radiation pressure balances that from the central planet, so the orbit does not evolve. In other configurations, these torques will not balance and the eccentricity and pericenter will change over time. For example, imagine that the orbit starts off with a small eccentricity $e_i < e_f$ and the pericenter located $+90°$ ahead of the subsolar longitude. At this time, the particle is heading away from the Sun at pericenter and is approaching the Sun at apocenter. The solar radiation pressure therefore causes the particle to accelerate in the direction of orbital motion when it is at pericenter and to decelerate at apocenter. This causes the orbit's eccentricity to increase (note that in Eq. 11, $F_t \cos f$ is positive in both positions). At the same time the pericenter precesses around the planet under the influence of Saturn's oblateness. The eccentricity continues to grow until the apocenter becomes aligned with the Sun. However, once the orbit's precession carries the apocenter further, toward the dusk ansa of the ring, the particle will be moving away from the Sun at apoapse and towards the Sun at periapse. At this point, the solar radiation pressure will accelerate the particle near apoapse and decelerate it near periapse, causing the eccentricity to shrink (note that in Eq. 11, $F_t \cos f$ is negative). The orbital eccentricity will therefore decrease until it reaches a minimum when the pericenter is aligned with the Sun, at which point the cycle begins anew.

Now consider the inclination and node. Consider a case where the Sun is in the southern hemisphere, the initial inclination $i_i > i_f$, and the ascending node is near the sub-solar longitude. At this time, the particle is heading northwards on the sunward side of its orbit and southwards on the shadowed side. The radiation force from the Sun pushes northwards on the particle as it passes on the sunward side of the planet, accelerating the vertical motion of the particle and increasing the inclination in the orbit. If there were no shadow, then this increased tilt would be cancelled out when the particle feels the same northward force as it

is heading southward on the planet's far side. However, because sunlight is blocked from this side of the rings by the planet's shadow, the torque is not cancelled and the inclination increases. Meanwhile, the node regresses due to Saturn's oblateness (if $i > i_f$, then the second term on the left hand side of Eq. 37 dominates). Thus the inclination continues to grow until the ascending node reaches a point 90° behind the Sun. After this point, the ascending node will head into the shadow and the descending node will move towards the sub-solar longitude. In this case, the particle is moving southwards while it is exposed to solar radiation pressure that drives it northwards, so the radiation pressure will decelerate the vertical motion and cause the inclination to lessen until it reaches a minimum when the ascending node is 90° ahead of the solar point, at which point the cycle starts again.

The orbital evolution described above is not specific to solar radiation pressure, but will occur whenever the ring particles feel forces with a fixed direction in inertial space. To demonstrate that solar radiation pressure in particular is a reasonable explanation for the shape and orientation of the Charming Ringlet, let us now evaluate numerically the strength of the solar radiation pressure force $F_\odot$ and the resulting e_f and i_f.

The solar radiation pressure force $F_\odot$ is given by (Burns *et al.* 1979):

$$F_\odot = SAQ_{pr}/c, \tag{51}$$

where c is the speed of light, S is the solar energy flux, A is the cross-sectional area of the particles, and Q_{pr} is an efficiency factor that is of order unity in the limit of geometric optics. The force ratio for quasi-spherical grains can therefore be written as:

$$\frac{F_\odot}{F_G} = \frac{3}{4}\frac{S}{c}\frac{a^2}{GM}\frac{Q_{pr}}{\rho r_g}, \tag{52}$$

where ρ is the particle's density and r_g is the particle's radius. If we now assume $S = 14$ W/m^2 at Saturn, $c = 3 * 10^8$ m/s, $GM = 3.8 * 10^{16}$ m^3/s^2, a =119,940 km (appropriate for the Charming Ringlet) and $\rho = 10^3$ kg/m^3 (appropriate for ice-rich grains) we find:

$$\frac{F_\odot}{F_G} = 1.3 * 10^{-5}\frac{Q_{pr}}{r_g/1\,\mu m}. \tag{53}$$

The other parameters in Eqs 38 and 40 can also be estimated. For the observations considered here, the shadow covers roughly 80° in longitude, so $\epsilon \simeq 0.2$, in which case $f(\epsilon) \simeq 0.85$ and $g(\epsilon) \simeq 0.2$. Also, given Saturn's gravitational harmonics (Jacobson *et al.* 2006), the orbital and precession rates in the vicinity of the Charming Ringlet are $n = 736°$/day and $\dot{\varpi}'_o \simeq |\dot{\Omega}'_o| \simeq 4.7°$/day. With these values, the forced eccentricities and inclinations are:

$$e_f \simeq 0.0026 \cos B_\odot \frac{Q_{pr}}{r_g/1\,\mu m}, \tag{54}$$

$$i_f \simeq 0.00041 \sin|B_\odot| \frac{Q_{pr}}{r_g/1\,\mu m}. \tag{55}$$

Note that over the course of Saturn's year, $\cos B_\odot$ ranges from 0.9 to 1.0, while $\sin|B_\odot|$ ranges from 0 to 0.5. Thus i_f can change significantly on seasonal time scales, while e_f should remain approximately constant.

The ae observed in the Charming Ringlet range between 10 and 30 km. This would be consistent with the e_f predicted by this model if r_g/Q_{pr} is between 10 and 30 microns, which are perfectly reasonable values. These findings therefore support the notion that solar radiation pressure influences this ringlet's dynamics.

The variations in the ringlet's eccentricity, pericenter and node relative to the Sun could potentially also be explained by this sort of model in terms of non-zero free eccentricities and inclinations. Indeed, we will show below that just such a model can provide a useful description of the ring's shape. However, at the same time, we must recall that the above analysis was for the orbital properties of a single particle, whereas the observed ringlet is composed of many particles. One would expect that these particles would have a range of sizes, and some dispersion in their orbital parameters. While the shape of the ringlet should reflect the average orbital parameters of all its constituent particles, one might have expected that this averaging would wash out any free component in the eccentricity or inclination. Such a model therefore raises a number of questions about the dynamics of this ringlet, which will be discussed in more detail below.

5. Combining the observations

Keeping in mind the above caveats about applying a model appropriate to an individual particle's orbit to the entire ringlet, we will now attempt to fit the observational data to a ten-parameter global model that includes both forced and free components in the eccentricity and inclination.

As discussed above, an orbit with forced and free orbital elements will trace out circles in $[h, k]$ and $[p, q]$ space as the orbit evolves. Therefore, we plot the orbital elements derived from the above fits in this space (see Fig. 6). Intriguingly, the admittedly sparse data do seem to describe a circle in $[h, k]$ space, centered roughly at $[ah, ak] = [-17, 0]$ km. In $[p, q]$ space, the situation is less clear. Neglecting the outlying data from Orbit 96 (discussed above), the data could be consistent with a circle centered near the origin, but most of the data points are clustered to one side of the circle, making it difficult to be certain.

To make these visual impressions more quantitative, we found the circles in $[h, k]$ and $[p, q]$ that best describe the data. We used the following procedures for the $[h, k]$ data: For each possible value of $[h, k]$, we computed the distance between this point and the location of every one of the longitudinal scan data points $[h_j, k_j]$:

$$R_j(h, k) = \sqrt{(h - h_j)^2 + (k - k_j)^2}. \tag{56}$$

(Note the data from the elevation scan are not included in this analysis because they do not constrain h and k or p and q separately). We also calculate a typical error for each data point σ_j, which is the average of the errors on h and k (the difference in the errors on these parameters was not considered large enough to justify complicating the analysis). We then compute the average value of the appropriate R_j, weighting the observations by their error

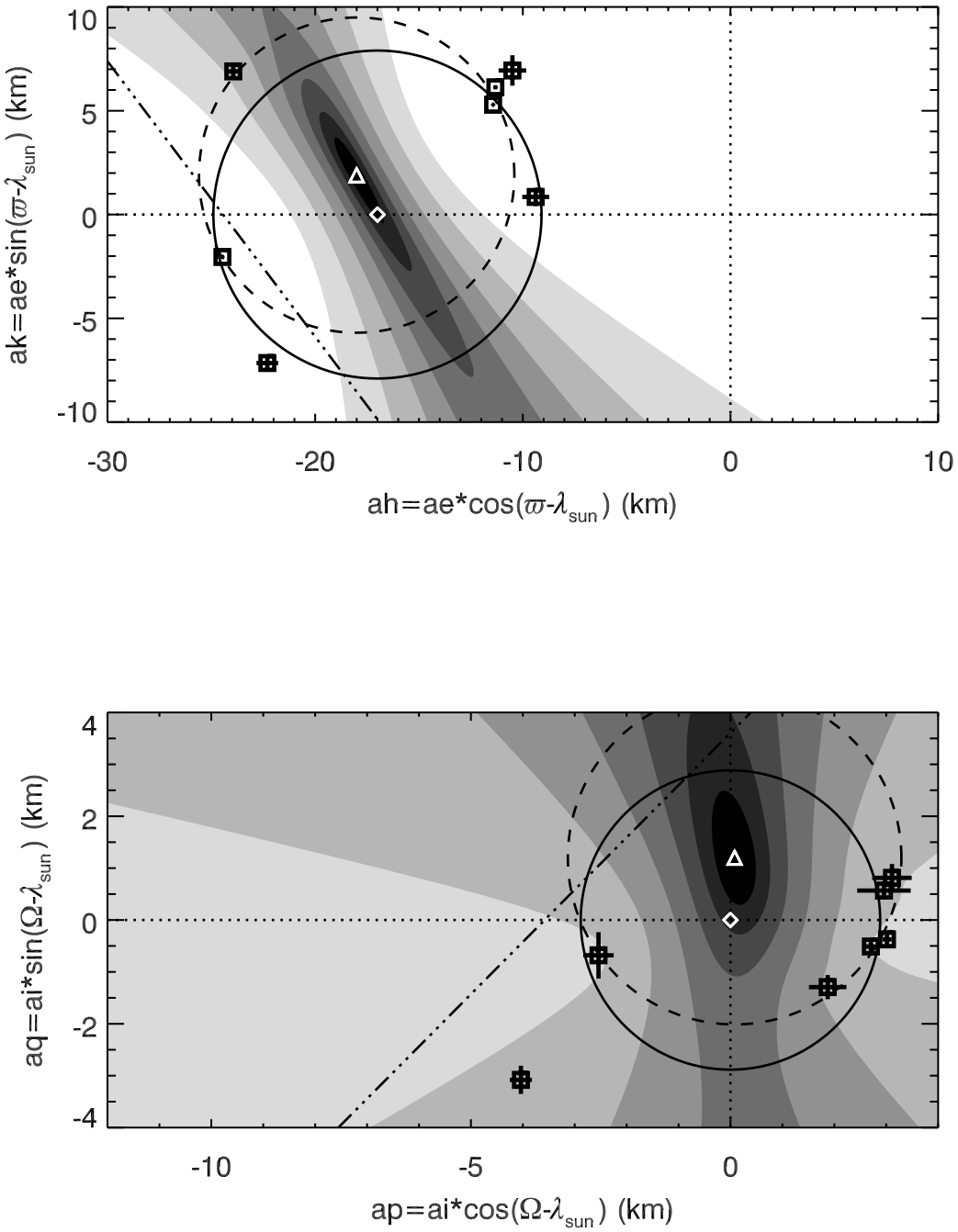

Fig. 6.— Diagrams showing the data derived from the various observations versus the parameters ah and ak (top) and ap and aq (bottom). The data points with error bars come from the longitudinal scans (see Table 2). The dot-dashed line represents the constraints from the elevation scan. The gray scales in the background indicate the values of the χ^2-statistic on the forced eccentricity and inclination discussed in the text. Each level corresponds to a factor of 2 in χ^2 (which dark being lower values). The white triangles mark the best-fit values of h, k, p and q. In the upper plot, the white diamond marks the best-fit forced eccentricity along the $k = 0$ axis, while in the lower plot the diamond is at the origin. The solid and dashed lines are the best-fit circles centered on the diamonds and triangles, respectively.

bars, to obtain the mean distance $\bar{R}$. We then compute the following χ^2 statistic:

$$\chi(h,k)^2 = \sum \frac{(R_j(h,k) - \bar{R})^2}{\sigma_j^2}. \tag{57}$$

This statistic measures the goodness of fit of the data to the best-fit circle centered at a given value of h and k. The $[p,q]$ space analysis is essentially the same, except that the data from Orbit 96 are excluded from the fit for the reasons described above. The contours in Fig. 6 illustrate how χ^2 varies with $[h,k]$ and $[p,q]$.

For the $[h,k]$ plot, the best-fit solution is at $[ah, ak] = [-18, 1.9]$ km. This would imply that the periapse leads the anti-solar direction by 6°. However, the best-fit solution assuming the pericenter is exactly anti-aligned with the Sun is not obviously worse than the overall best fit. Note that even for these best-fitting models, the χ^2 fit is still quite poor (74 for 4 degrees of freedom). This is consistent with a visual inspection of the data, which scatter around the circle by more than their error bars. This excess scatter could occur for a number of reasons. The data used here come from a range of phase angles and are sensitive to different parts of the size distribution, which may lead to differences in the apparent shape of the ringlet. Also, our background subtraction algorithm and other procedures used to derive the radial positions of the ringlet may have introduced systematic errors between different scans.

For the $[p,q]$ plot, the best-fitting model has $[ap, aq] = [0, 1.2]$ km. Here the χ^2 value is good (3.1 for 3 degrees of freedom). However, the difference in the quality of the fit between this and $[p,q] = [0,0]$ is only marginally significant (assuming no forced inclination, the χ^2 is 9.9 for 5 degrees of freedom). Furthermore, since the Sun is in the southern hemisphere, and $B_\odot$ is negative, we expect that the best-fit q should be negative, not positive. Thus the best-fitting model is a bit of a surprise. Since $B_\odot$ changes significantly over the time period covered by these observations, a more complete model would include a time-variable forced inclination. However, given the weak evidence for any forced inclination at all, we chose not to consider such complications at this time.

Despite these uncertainties, we can now explore whether the temporal evolution of the shape parameters are consistent with the above model, which suggests that the parameters should drift around the circles at nearly constant rates determined by the modified pericenter-precession and nodal-regression rates. Given the sparseness of the data, we cannot establish easily whether any given solution is unique. However, preliminary examination of the data showed that they were approximately consistent with the expected drift rates ($\dot{\varpi}'_o \simeq -\dot{\Omega}'_o \simeq 4.7°$/day). Therefore, for each posssible solution for e_f, e_l, i_f and i_l, we determined the phase of the shape for each longitudinal-scan observation, unwrapped the phase assuming drift rates close to those expected, and fitted the resulting phases versus observation time to a line to obtain estimates of the rates $\dot{\varpi}'_l$ and $\dot{\Omega}'_l$, as well as the longitudes at epoch ϖ'_l and Ω'_l (the epoch time being taken as the time of the first image in the Orbit 42 sequence 2007-099T22:19:10, see Table 1). Regardless of whether we accepted the best-fit solution (triangles/dashed circles in Fig 6) or a simplified solution assuming $\varpi'_f = 180°$ and $i_f = 0$ (diamonds/solid circles in Fig 6), we obtain roughly the same rates.

$\dot{\varpi}'_l = 4.66°$/day and $\dot{\Omega}'_l = -4.75°$/day. Recall that these are the modified precession rates in a reference frame tied to the Sun. The precession rates in an inertial coordinate system must account for the movement of Sun $\dot{\lambda}_\odot = 0.03°$/day. Thus the precession rates are actually: $\dot{\varpi}_l = 4.69°$/day and $\dot{\Omega}_l = -4.72°$/day. The expected rates at 119940 km are 4.71°/day and -4.68°/day, respectively, so these numbers are close to theoretical expectations. This model therefore can provide a useful parametrization of the available data.

Table 3 summarizes the model parameters for the shape of the Charming Ringlet. Model 1 is the simplified model in which ϖ_f is taken to be exactly anti-aligned with the Sun and the forced inclination is assumed to be zero. Model 2 is the more complex model that allows both ϖ'_f and i_f to have their "best-fit" values.

Table 3: Model parameters for the Charming Ringlet

Model	ae_f (km)	ϖ'_f (deg)	ae_l [a] (km)	$\dot{\varpi}'_l$ [b] (deg/day)	ϖ'_l [b,c] (deg)	ai_f (km)	Ω'_f (deg)	ai_l [a] (km)	$\dot{\Omega}'_l$ [b] (deg/day)	Ω'_l [b,c] (deg)
1	17.0±0.5[d]	180	7.9±0.4	4.66±0.01	230±3	–	–	2.9±0.2	-4.73±0.02	-152±9
2	18.1	174	7.6±0.4	4.67±0.01	225±4	1.3	+90	3.3±0.1	-4.77±0.02	-158±9

[a] Errors are the standard deviations of the values R_j, see Eqn 56.

[b] Errors from linear fit, assuming central values for ae_f, ae_l, ai_f and ai_l

[c] Longitudes relative to Sun at epoch=2007-099T22:19:10 (time of first observation in Orbit 042).

[d] Error based on factor of 2 increase in χ^2 relative to best-fit value

Note Rev 96 data excluded from inclination/node fits.

Table 4: Comparison of model predictions for eccentricity and pericenter with observed longitudinal scan data

Orbit/Obs. Sequence	ae (km) Observed	ae (km) Model 1	ae (km) Model 2	Observed-Model 1	Observed-Model 2	ϖ' (deg) Observed	ϖ' (deg) Model 1	ϖ' (deg) Model 2	Observed-Model 1	Observed-Model 2
030/AZDKMRHP001/	24.9	23.3	23.5	+1.6	+0.8	163.9	166.1	161.1	-2.1	+2.9
042/RETMDRESA001/	23.4	22.9	23.9	+0.5	-0.2	197.8	195.3	188.6	+2.5	+9.2
070/RETMDRESA001/	9.4	9.4	10.7	+0.0	-1.7	174.8	170.0	161.9	+4.9	+12.9
071/PAZSCN002/	12.5	13.2	14.1	-0.6	-2.4	146.5	153.3	149.7	-6.8	-3.2
082/RETARMRLP001/	12.9	13.8	14.9	-0.9	-2.8	151.6	152.7	149.3	-1.1	+2.3
092/RETARMRLF001/	12.6	12.2	13.4	+0.4	-1.6	155.2	154.9	150.5	+0.2	+2.6
096/RETARMRMP001/	24.6	24.9	25.5	-0.3	-1.0	184.8	182.2	178.3	+2.6	+6.5
Mean				+0.11	-1.27				+0.02	+5.04
St. Dev.				0.86	1.29				3.85	5.19

Table 5: Comparison of model predictions for inclination and node with observed longitudinal scan data

Orbit/Obs. Sequence	ai (km) Observed	ai (km) Model 1	ai (km) Model 2	Observed-Model 1	Observed-Model 2	Ω' (deg) Observed	Ω' (deg) Model 1	Ω' (deg) Model 2	Observed-Model 1	Observed-Model 2
030/AZDKMRHP001/	2.3	2.9	2.6	-0.6	-0.3	325.3	316.1	337.5	+9.3	-12.7
042/RETMDRESA001/	2.6	2.9	3.1	-0.3	-0.4	195.0	207.7	179.2	-12.7	+15.8
070/RETMDRESA001/	3.2	2.9	3.9	+0.3	-0.6	14.6	33.1	33.1	-18.5	-18.5
071/PAZSCN002/	3.0	2.9	3.1	+0.1	-0.1	10.9	-4.0	-0.4	+14.8	+11.2
082/RETARMRLP001/	3.0	2.9	2.8	+0.1	+0.3	352.9	345.0	345.3	+7.9	+7.6
092/RETARMRLF001/	2.8	2.9	2.8	+0.1	-0.1	349.3	351.9	350.2	-2.5	-0.8
096/RETARMRMP001/	5.1	2.9	3.6	+2.2	+1.5	217.3	203.3	156.8	+14.1	+60.5
Mean (excluding 096 data)				-0.06	-0.21				-0.28	+0.53
St. Dev. (excluding 096 data)				0.34	0.33				13.24	13.54

Table 6: Comparison of model predictions with elevation scan observation

	ae (km)	ϖ' (deg)	ai (km)	Ω' (deg)	C (km/rad)	z
Observation					19.5	2.54
Model 1	24.3	188.2	2.9	237.7	22.0	2.78
Model 2	25.2	186.2	2.4	216.6	22.4	2.37

6. Comparing model predictions with the observations

Tables 4, 5 and 6 compare the observed shape parameters measured by the various observations with the predictions from the two models derived above. While the model parameters were derived using weighted averages of data from different observations, these comparisons do not consider variations in the uncertainties in the observations. This is because, as noted above, these simplified models were unable to fit the $[h, k]$ data to within the error bars. Thus an unweighted analysis will provide a conservative estimate of how well these models describe the data.

Table 4 presents the model predictions for the eccentricity and pericenter locations from the longitudinal scans. Note that the only observation where the more complex Model 2 does a better job predicting the eccentricity and pericenter than the simpler Model 1 is in the Orbit 30 data. This is consistent with Fig 6, where the dashed circle (Model 2) gets closer to the point in the upper left (from Orbit 30) than the solid circle (Model 1), but for all the other data points the dashed circle is not obviously a better fit than the solid one. Note the Orbit 30 data were taken at a substantially higher phase angle than the other observations, so this observation may probe a different part of the size distribution and the shape parameters may not be perfectly comparable to the others. Therefore, we conclude that the simpler model that assumes the forced component of the pericenter is perfectly anti-aligned with the Sun is a preferable model for the shape of the ring. This model recovers the eccentricity of the ringlet with an *rms* residual of 1 km and the pericenter location with an *rms* residual of 4°.

Table 5 presents the model predictions for the inclinations and nodes for the longitudinal scans. In this case, there is not a clear difference between the two models. Given that including a forced inclination does not substantially reduce the scatter in the observations, for the sake of simplicity we favor the use of the simpler Model 1 in this case as well. Here the model predicts the inclination with an *rms* residual of 0.3 km and the node location with an *rms* residual of 14°.

Finally, Table 6 compares the model predictions for the z and C parameters for the elevation scan (see Eqs 7 and 8). This is a critical check on the model, which was developed using only the longitudinal scan data. Here, we can see that both models give values for z and C that are reasonably consistent with the observed values.

In conclusion, while Model 1 is clearly over-simplified and does not provide a perfectly accurate description of the observed data, it nevertheless appears to be a useful approximate description of the ringlet's shape and time variability.

7. Interpretation

We can now compare the observed shape parameters of this ringlet with theoretical expectations. The *forced* eccentricity and inclination can be relatively easily understood in terms of the solar radiation forces discussed above. By contrast, the *free* components of the

eccentricity and inclination are surprising and more difficult to explain.

7.1. Forced eccentricity and inclination

Equations 54 and 55 indicate that solar radiation pressure should produce a ring with $i_f/e_f \simeq 0.16 \tan|B_\odot|$. For the observations described here $|B_\odot|$ ranges between 16° and 3°, so i_f/e_f would be between 0.04 and 0.01. This is consistent with the observed values of $ae_f \simeq 17$ km and $ai_f < 1$ km. Furthermore, the observed ae_f suggests a typical particle size $r_g \simeq 20\mu\text{m}*Q_{pr}$, which is not unreasonable. However, we must caution that the particles in the Charming Ringlet probably have a distribution of sizes, and this estimated value of r_g may only be an effective average value for this distribution. The particle size distribution will be investigated in more detail in a future study of the ring's spectrophotometric properties and detailed morphology.

7.2. Free eccentricity and inclination

While nonzero free eccentricities and inclinations are acceptable solutions to the equation of motion for a single particle's orbit, it is surprising for the ringlet as a whole to exhibit such terms, because they imply that all the component particles' orbits not only have comparable finite values of e_l and i_l, but also have similar values of ϖ_l and Ω_l. Such an asymmetry in these components of the ring's shape could be due to one of three things: (1) an asymmetry in the initial conditions of the ring particles, (2) an explicit longitudinal asymmetry in the equations of motion, or (3) a spontaneous symmetry-breaking in the ringlet. We will consider each of the possibilities below.

7.2.1. Asymmetric initial conditions

There are various ways to produce a collection of particles with the same values for ϖ_l and Ω_l. For example, an impact near the present location of the ringlet could release a cloud of dust from one point in space, suddenly injecting a collection of particles into the gap that have similar orbital elements. Alternatively, particles could be supplied into the ring over an extended period of time, but for some reason dust grains with certain orbital parameters are generated at higher rates than others. In this case, the relevant source bodies for the dust would almost certainly be too large to have any detectable forced eccentricity due to solar radiation pressure. Thus the observed heliotropic ring could not be simply be low-velocity impact debris tracing the orbit of its source material, but instead must reflect some more complex production process involving various interactions with the local plasma and dust environment.

Regardless of how the particles were injected into the ring, the observable ring particles must be relatively young in order for any asymmetry in the initial conditions to be visible

in the present ringlet. The Charming Ringlet has a full-width at half-maximum of about 30 km. If we assume a comparable spread in semi-major axes, then the precession rates of the particles in the ring will vary by about 0.003°/day. The values of ϖ_l and Ω_l would therefore spread over all possible longitudes in a few hundred years. While this time-scale could be extended if we assume the radial width of the ring is due to variable eccentricities rather than semi-major axes, even then the visible particles in the ring probably cannot be more than a few thousand years old if they are to preserve any asymmetry in their initial conditions. Such ages are not entirely unreasonable, for small dust grains like those seen in the Charming Ringlet can be rapidly destroyed by energetic particle bombardment (Burns *et al.* 2001), or lost by adhering to larger objects in the Cassini Division. However, we must caution that the production and loss of dust grains within narrow gaps has not been studied in great detail yet.

Another important constraint on these sorts of models is the lack of gross variations in the brightness or morphology of the ring with longitude. This argues against any large source bodies existing within the ringlet itself, as such objects would tend to scatter and perturb the material in their vicinity, producing either gaps or possibly clumps similar to those visible in the Encke gap ringlets; such gaps and clumps are not seen in the Charming Ringlet. It also requires that the ringlet grains exist long enough to spread evenly over all longitudes, which takes a few years or decades.

7.2.2. Asymmetric terms in the equations of motion

Instead of an asymmetric source, it is also conceivable that the equations of motion contain terms that depend on ϖ_l and Ω_l. Recently, Hedman *et al.* (2010) demonstrated that a combination of perturbations from Mimas and the massive B-ring outer edge could give rise to terms in the equation of motion like:

$$\left\langle \frac{d^2\varpi}{dt^2} \right\rangle = -f_o^2 \sin(\varpi - \dot{\varpi}_r t), \tag{58}$$

where f_o and $\dot{\varpi}_r$ are constants. Such a term acts as a restoring force on the pericenter location of any particle's orbit. Thus, in a region where the precession rate $\dot{\varpi} \simeq \dot{\varpi}_r$, this term aligns the pericenters of all freely-precessing eccentric orbits. If such a term was effective on the Charming Ringlet, it could explain how all the particles in the ringlet happen to have the same value of ϖ_l.

One difficulty with this sort of model is that the particles in the Charming Ringlet seem to have both ϖ_l and Ω_l aligned. While one could imagine expressions similar to Eqn 58 involving the node instead of the pericenter, it is difficult to have both terms operate at the same location. Like any other resonant term in the equations of motion, such terms can only be effective over a narrow range of semi-major axes (or equivalently, narrow ranges of $\dot{\varpi}$ and/or $\dot{\Omega}$), and resonances involving nodes typically occur at different locations from those involving pericenters (Murray and Dermott 1999). It therefore would be quite a coincidence if the Charming Ringlet just happened to fall at a location where both angles

could be effectively constrained.

7.2.3. Spontaneous symmetry breaking

A ringlet with finite free eccentricity and free inclination can in principle form spontaneously without any terms in the equations of motion that depend explicitly on ϖ_l and Ω_l, and without any strong asymmetry in the particle's initial conditions. Such phenomena have been discussed almost exclusively in the context of massive, dense ringlets (Borderies *et al.* 1985). However, one can argue that this sort of "spontaneous symmetry-breaking" could also occur in low-optical-depth dusty rings via dissipative processes like collisions, provided that there are terms in the individual particle's equations of motion that favor the development of a nonzero e_l and i_l comparable to those observed for the entire ringlet.

Dissipative collisions are often invoked as a mechanism that causes narrow rings to spread in semi-major axis (Goldreich and Tremaine 1982), so it might seem surprising that such collisions could also align pericenter or node locations. However, unlike the semi-major axis, the longitudes of pericenter and node have no direct effect on a particles' orbital energy. Thus, while the dissipation of orbital energy requires that particles' orbital semi-major axes evolve in a particular direction, this is not the case for pericenters or nodes. Instead, the evolution of pericenters and nodes should be driven primarily by the collisons' dissipation of relative motions.

To illustrate how such collisions can align pericenters and nodes, consider the following simple situation: There is a ringlet composed of many particles with similar orbital properties, and there is a single particle whose orbit is misaligned with the others. For simplicity, assume that both the ringlet and the particle have zero eccentricity and zero forced inclination. Furthermore, assume that both the ringlet and the particle have the same free inclination i but different longitudes of ascending node Ω_r and Ω_p, respectively. If $\Omega_r \neq \Omega_p$, then the particle's orbit will cross the ringlet at two longitudes $\lambda_c = (\Omega_p + \Omega_r)/2 \pm \pi/2$. At these two longitudes the particle will feel a force due to its collisions with the particles in the ringlet, and the vertical component of that force F_z will be proportional to the vertical velocity of the particles in the ringlet, so $F_z \propto \cos(\lambda_c - \Omega_r)$. Inserting this into Equation 14, we can express the perturbation to the particle's node position due to its interactions with the ringlet as:

$$\frac{d\Omega_p}{dt} = 2D \sin(\lambda_c - \Omega_p) \cos(\lambda_c - \Omega_r) \tag{59}$$

where D is a constant. Substituting in the above expression for the crossing longitudes λ_c and simplifying, this expression reduces to the simple form:

$$\frac{d\Omega_p}{dt} = -D \sin(\Omega_p - \Omega_r). \tag{60}$$

The forces applied to the particle's orbit during the ringlet crossings therefore do tend to align the particle's orbital node position with that of the ringlet. A similar calculation demonstrates that the same basic phenomenon acts to align pericenters as well. Thus colli-

sions can indeed align pericenters and nodes, provided the collisions are frequent (and lossy) enough, and provided the particles maintain some finite (free) eccentricity and inclination.

The requirement that collisions are frequent enough to align pericenters is probably met for the Charming Ringlet. While this ringlet has a low normal optical depth (roughly 10^{-3}), the orbital period is sufficiently short (around 0.5 days) that the collisional timescale is still only a few years or decades, much less than the typical erosion timescales of thousands of years (Burns *et al.* 2001).

On the other hand, the persistance of the nonzero free eccentricities and inclinations probably requires some modifications to the individual particles' dynamics. If the particles' equations of motion were just given by Eqs 47- 50 above, dissipative collisions would (assuming the initial conditions were not highly asymmetric) tend to produce a ringlet with $e_l = i_l = 0$. Thus, we probably need to add some additional terms to these equations to produce something similar to the Charming Ringlet's observed shape. One relatively simple way to accomplish this is to add non-linear damping terms into the equations:

$$\left\langle \frac{dh}{dt} \right\rangle = -\dot{\varpi}'_o k + \gamma_h (h + e_f) \left[1 - \left(\frac{h + e_f}{e_l} \right)^2 \right], \tag{61}$$

$$\left\langle \frac{dk}{dt} \right\rangle = \dot{\varpi}'_o (h + e_f) + \gamma_k k \left[1 - \left(\frac{k}{e_l} \right)^2 \right], \tag{62}$$

$$\left\langle \frac{dp}{dt} \right\rangle = -\dot{\Omega}'_o \left(q - i_f \frac{B_\odot}{|B_\odot|} \right) + \gamma_p p \left[1 - \left(\frac{p}{i_l} \right)^2 \right], \tag{63}$$

$$\left\langle \frac{dq}{dt} \right\rangle = \dot{\Omega}'_o p + \gamma_q \left(q - i_f \frac{B_\odot}{|B_\odot|} \right) \left[1 - \left(\frac{q - i_f B_\odot / |B_\odot|}{i_l} \right)^2 \right], \tag{64}$$

where $\gamma_h, \gamma_k << \dot{\varpi}'_o$ and $|\gamma_p|, |\gamma_q| << |\dot{\Omega}'_o|$ quantify the magnitude of the damping terms. These terms transform the $[h, k]$ and $[p, q]$ systems from simple harmonic oscillators into van der Pol oscillators (Baierlein 1983). Such oscillators are characterized by a limit cycle which the system will asymtotically approach no matter where it is started in $[h, k]$ and $[p, q]$ space. These limit cycles are circles centered at $[h, k] = [-e_f, 0]$ and $[p, q] = [0, \pm i_f]$ with radii of e_l and i_l, and the orbit traces out the circles at rates given by $\dot{\varpi}'_o$ and $\dot{\Omega}'_o$. These equations of motion therefore cause any particle's orbit to evolve to the same path as the observed ringlet. On their own, particles started at different points in phase space will wind up at different points along this cycle. However, if the relative motions among the particles are efficiently dissipated, then all the particles should eventually clump together in phase space such that they all move around the limit cycle together, as observed.

Models of this sort have the advantage that the additional terms in the equations of motion do not have explicit frequency-dependent terms that can only be effective at specific locations in the rings. Such terms are therefore more likely to show up in a broader range of contexts, and could even be generic features of small dust grains' dynamics in narrow gaps. For example, the nonlinear damping terms in the above equations contain either e_l or i_l. While these are small numbers in absolute terms, they are not much smaller than the

fractional gap width $\delta a/a$, so such factors could arise due to interactions between the ringlet particles and the gap edges. This would not be unreasonable, as small particles could be attracted to the edges by the force of gravity, or even repelled if the small grains in the ring have a sufficient electrical charge. Furthermore, variations in the plasma environment within the gap could also possibly produce perturbations on the grains' motions with the appropriate positional dependence.

One clue to the exact nature of these forces is that the observed ring traces out a circle that is centered on the point $[h, k] = [-e_f, 0]$ and excludes the origin $[h, k] = [0, 0]$. Based on some preliminary analyses, it appears that a limit cycle of this type cannot be created by non-linear damping terms involving only e or ϖ , but instead requires terms that contain k and/or $h + e_f$, like the ones given above (note that only one of the two terms γ_h and γ_k has to be non-zero to produce the desired limit cycle). Since h and k are tied to the location of the Sun, this implies that these damping terms might also have some connection with the Sun. One possibility is that these terms reflect the influence of Saturn's shadow. When small particles enter the shadow, electrons are no longer being ejected from their surfaces via the photoelectric effect. This can significantly change their electric charge and thereby lead to significant forces that would preferentially damp or drive h or k. Further investigation is needed to explore whether the perturbations from these or other processes could account for the observed shape of the Charming Ringlet.

Acknowledgments

We acknowledge the support of NASA, the Cassini Project and the Imaging Science Team for obtaining the images used in this analysis. This work was also supported by Cassini Data Analysis Program grants NNX07AJ76G and NNX09AE74G. We wish to thank P.D. Nicholson and M.R. Showalter for useful conversations, and S. Charnoz and J. Schmidt for their helpful reviews of this manuscript.

Appendix: Orbit averages including shadow effects

Equations 23-27 are derived from Equations 18-22 by averaging over all longitudes λ. This averaging procedure is complicated by the presence of Saturn's shadow, which blocks sunlight from reaching part of the rings. If a fraction ϵ of the ring is in Saturn's shadow, then the ring particles only feel the solar radiation pressure when $|\lambda - \lambda_\odot| < \pi(1-\epsilon)$. Thus if X is any of the radiation-pressure-induced terms on the right-hand sides of Eqs 18-22, then the orbit-averaged value of X is:

$$< X >= \frac{1}{2\pi} \int_{-\pi(1-\epsilon)}^{+\pi(1-\epsilon)} X d(\lambda - \lambda_\odot). \tag{65}$$

Equations 18-22 contain terms proportional to λ^0, $\sin(\lambda - \lambda_\odot)$, $\sin(2\lambda - \varpi - \lambda_\odot)$, $\cos(2\lambda - \varpi - \lambda_\odot)$, $\sin(\lambda - \Omega)$, and $\cos(\lambda - \Omega)$. Inserting these factors into Eqn 65 yields

the following expressions:

$$< \lambda^0 >= (1 - \epsilon), \tag{66}$$

$$< \sin(\lambda - \lambda_\odot) >= 0, \tag{67}$$

$$< \sin(\lambda - \Omega) >= -\frac{\sin(\pi\epsilon)}{\pi} \sin(\Omega - \lambda_\odot), \tag{68}$$

$$< \cos(\lambda - \Omega) >= +\frac{\sin(\pi\epsilon)}{\pi} \cos(\Omega - \lambda_\odot), \tag{69}$$

$$< \sin(2\lambda - \varpi - \lambda_\odot) >= +\frac{\sin(2\pi\epsilon)}{2\pi} \sin(\varpi - \lambda_\odot), \tag{70}$$

$$< \cos(2\lambda - \varpi - \lambda_\odot) >= -\frac{\sin(2\pi\epsilon)}{2\pi} \cos(\varpi - \lambda_\odot). \tag{71}$$

The appropriate combination of these terms then yields the factors $d(\epsilon)$, $f(\epsilon)$ and $g(\epsilon)$ in Eqs 23-27.

REFERENCES

Baierlein, R. 1983. *Newtonian Dynamics*. McGraw-Hill.

Borderies, N., P. Goldreich, and S. Tremaine 1985. A granular flow model for dense planetary rings. *Icarus* **63**, 406–420.

Burns, J. A. 1976. Elementary derivation of the perturbation equations of celestial mechanics. *American Journal of Physics* **44**, 944–949.

Burns, J. A., D. P. Hamilton, and M. R. Showalter 2001. Dusty rings and circumplanetary dust: Observations and simple physics. In E. Grün, B. Gustafson, S. Dermott, and H. Fechtig (Eds.), *Interplanetary Dust*, pp. 641–725. Springer.

Burns, J. A., P. L. Lamy, and S. Soter 1979. Radiation forces on small particles in the solar system. *Icarus* **40**, 1–48.

Burt, J., M. M. Hedman, M. S. Tiscareno, and J. A. Burns 2008. The where And why Of Saturn's inclined "Charming Ringlet". *BAAS* **40**, 445.

French, R. G., E. A. Marouf, N. J. Rappaport, and C. A. McGhee 2010. Occultation observations of Saturn's B ring and Cassini Division. *AJ* **139**, 1649–1667.

French, R. G., P. D. Nicholson, M. L. Cooke, J. L. Elliot, K. Matthews, O. Perkovic, E. Tollestrup, P. Harvey, N. J. Chanover, M. A. Clark, E. W. Dunham, W. Forrest, J. Harrington, J. Pipher, A. Brahic, I. Grenier, F. Roques, and M. Arndt 1993. Geometry of the Saturn system from the 3 July 1989 occultation of 28 SGR and Voyager observations. *Icarus* **103**, 163–214.

Goldreich, P., and S. Tremaine 1982. The dynamics of planetary rings. *ARA&A* **20**, 249–283.

Hamilton, D. P. 1993. Motion of dust in a planetary magnetosphere - Orbit-averaged equations for oblateness, electromagnetic, and radiation forces with application to Saturn's E ring. *Icarus* **101**, 244–264.

Hedman, M. M., J. A. Burns, M. S. Tiscareno, and C. C. Porco 2007. The Heliotropic Rings of Saturn. *BAAS* **38**, 427.

Hedman, M. M., P. D. Nicholson, K. H. Baines, B. J. Buratti, C. Sotin, R. N. Clark, R. H. Brown, R. G. French, and E. A. Marouf 2010. The architecture of the Cassini Division. *AJ* **139**, 228–251.

Horányi, M., and J. A. Burns 1991. Charged dust dynamics - Orbital resonance due to planetary shadows. *J. Geophys. Res.* **96**, 19283–19289.

Horányi, M., J. A. Burns, M. M. Hedman, G. H. Jones, and S. Kempf 2009. Diffuse Rings. In Dougherty, M. K., Esposito, L. W., & Krimigis, S. M. (Ed.), *Saturn from Cassini-Huygens*, pp. 511–536. Springer.

Jacobson, R. A., P. G. Antreasian, J. J. Bordi, K. E. Criddle, R. Ionasescu, J. B. Jones, R. A. Mackenzie, M. C. Meek, D. Parcher, F. J. Pelletier, W. M. Owen, Jr., D. C. Roth, I. M. Roundhill, and J. R. Stauch 2006. The Gravity Field of the Saturnian System from Satellite Observations and Spacecraft Tracking Data. *AJ* **132**, 2520–2526.

Murray, C. D., and S. F. Dermott 1999. *Solar System Dynamics*. Cambridge University Press.

Porco, C. C., E. Baker, J. Barbara, K. Beurle, A. Brahic, J. A. Burns, S. Charnoz, N. Cooper, D. D. Dawson, A. D. Del Genio, T. Denk, L. Dones, U. Dyudina, M. W. Evans, B. Giese, K. Grazier, P. Helfenstein, A. P. Ingersoll, R. A. Jacobson, T. V. Johnson, A. McEwen, C. D. Murray, G. Neukum, W. M. Owen, J. Perry, T. Roatsch, J. Spitale, S. Squyres, P. Thomas, M. Tiscareno, E. Turtle, A. R. Vasavada, J. Veverka, R. Wagner, and R. West 2005. Cassini imaging science: Initial results on Saturn's rings and small satellites. *Science* **307**, 1226–1236.

Porco, C. C., R. A. West, S. Squyres, A. McEwen, P. Thomas, C. D. Murray, A. Delgenio, A. P. Ingersoll, T. V. Johnson, G. Neukum, J. Veverka, L. Dones, A. Brahic, J. A. Burns, V. Haemmerle, B. Knowles, D. Dawson, T. Roatsch, K. Beurle, and W. Owen 2004. Cassini imaging science: Instrument characteristics and anticipated scientific investigations at saturn. *Space Science Reviews* **115**, 363–497.

Porco, C.C. and the Cassini Imaging Team. 2006. Rings of Saturn (R/2006 S 1, R/2006 S 2, R/2006 S 3, R/2006 S 4). *IAU Circ.* **8759**, 1.